Tailored Topological Edge Waves via Chiral Hierarchical Metamaterials

Jacopo M. De Ponti[1,*] Luca Iorio[1] Gregory J. Chaplain[2] Alberto Corigliano[1]
Richard V. Craster,[3,4,5] and Raffaele Ardito[1]

[1]*Department of Civil and Environmental Engineering, Politecnico di Milano, Piazza Leonardo da Vinci, 32, Milano 20133, Italian Republic*

[2]*Department of Physics and Astronomy, Centre for Metamaterial Research and Innovation, University of Exeter, Exeter EX4 4QL, United Kingdom*

[3]*Department of Mathematics, Imperial College London, London SW7 2AZ, United Kingdom*

[4]*Department of Mechanical Engineering, Imperial College London, London SW7 2AZ, United Kingdom*

[5]*Abraham de Moivre International Research Laboratory, Imperial College London, London SW7 2AZ, United Kingdom*

Precise manipulation of the direction and redirection of vibrational wave energy is a key demand in wave physics and engineering. We consider the paradigm of a finite framelike structure and the requirement to channel energy away from critical regions, leaving them vibration free, and redirect energy along edges toward energy concentrators for damping or energy harvesting. We design an exemplar frame metamaterial, combining two distinct areas of wave physics. First, we consider topological edge states, taking an unconventional tetrachiral lattice. We control these highly localized protected edge states leveraging a hierarchy of scales through the addition of microresonators that impose tunable symmetry breaking and reconfigurable mass. This allows us to achieve precise positional control in the macroscale frame lattice, thereby opening up opportunities for robust signal transport and vibration control. Experiments, theory, and simulation are all utilized to provide a comprehensive analysis and interpretation of the physics.

I. INTRODUCTION

The investigation of topological states of matter has attracted growing interest, with multiple realizations in photonics [1–4] and phononics [5,6]. From their initiation in the field of topological insulators in quantum-mechanical systems [7,8], protected edge (or interfacial) surface states have now percolated into the physical platforms of classical wave propagation. In the context of elasticity and acoustics, various topology-based mechanisms have been investigated, including nonreciprocity [9], wave pumping [10], one-way edge waves [11], and beam splitting [12], to name a few; an attractive property surrounding protected edge states is related to their resilience to backscattering and disorder [13], making them particularly important for signal transport and wave control [14]. Protected bands exist within bulk band gaps and stem from broken symmetries within a periodic system; the topological nature of the Bloch bands is defined by topological invariants, most notably the Berry phase [15–18] and the Chern number [19]. The nature of the

symmetry breaking delineates two classes of topological insulators, which are related to the preservation of time reversal symmetry (TRS). Active topological materials [11,20,21] have been inspired by the quantum Hall effect (QHE), where time-reversal symmetry (TRS) is broken by external fields [22]. Conversely, passive topological materials [5,13,23,24] have originated from the quantum spin Hall effect (QSHE) [25,26], where symmetry breaking is achieved by spin-orbit interactions (TRS is preserved). More recently, a number of studies have exploited valley degrees of freedom to achieve quantum valley Hall effect (QVHE) analogs [27–31] in classical wave systems. QVHE relies on the breaking of space-inversion symmetry (SIS), while maintaining TRS. This is an important difference with respect to QHE and QSHE that permits realistic applications (which do not require complex mechanisms to achieve TRS breaking) and this is particularly appealing for vibrational wave control.

Within the passive-topological-materials framework, we tailor protected edge states in an elastic frame constructed from unit cells (see Figs. 1 and 2). Given the necessity of developing edge modes that propagate in the frequency region defined by the band gaps of the bulk modes, we opt for a tetrachiral structure that allows for large band gaps
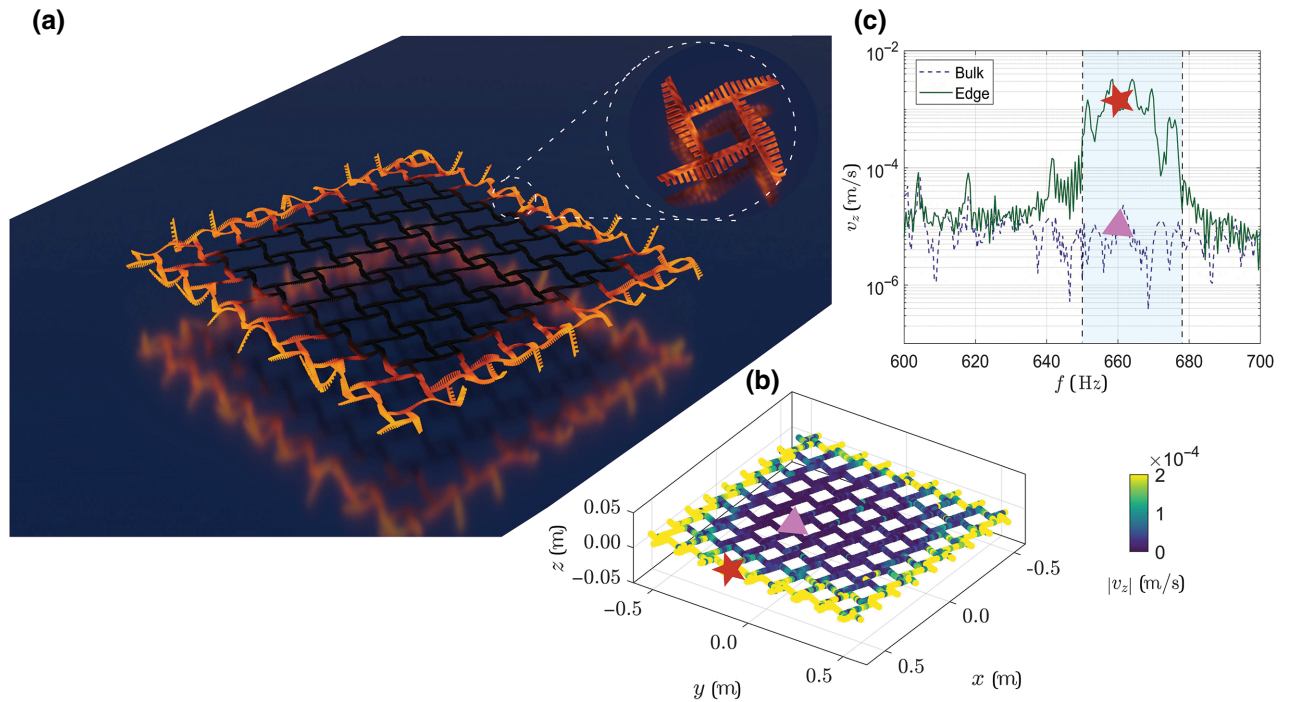

FIG. 1.   (a) Rendering from the numerical solution of the displacement field of the edge mode at the boundary of the lattice, together with an enlargement on the unit cell. The lattice is excited using an out-of-plane force on the edge, which is able to activate flexural-wave propagation. (b) Experimental results obtained with a scanning laser Doppler vibrometer (SLDV) on the real specimen, confirming strong agreement with numerical simulations. Experimental tests are performed by suspending the structure on a frame and providing the input using an electrodynamic shaker. (c) The logarithmic amplitude of the experimental displacement field, depending on the frequency. The two curves report the bulk (blue) and the edge (green) solutions. The dashed vertical lines denote the central part of the bulk band gap.

in the low-frequency spectrum [32,33]. We demonstrate that tetrachiral lattices possess not only distinctive static features but also nontrivial topological states motivated by the extension of well-known topological properties of hexagonal lattices to square lattices [34–39]. In addition, the obtained edge states can be precisely tuned leveraging graded arrays of masses within each unit cell. By doing so, we introduce a hierarchy of levels allowing us to design the internal microstructure of the unit cell to obtain highly controllable edge bands. Control over low-frequency vibration is both challenging and of practical importance. We are drawn to lightweight frame metamaterials that enable such control over a low-frequency operating range and the result is a candidate structure for addressing practical situations involving vibration isolation in ultraprecision machining [40], energy harvesting [41], and lossless signal transport for sensing applications [42].

Separate from topological wave physics, another recent advance has been to take photonic or phononic crystals and then grade them spatially to create rainbow trapping [43–47] or reflection devices [48–50]. Once robust edge states are established, the combination of these with such graded structures fulfills a requirement of vibrational devices, that is, to deliver maximum energy to preallocated

positions within the lattice. The combination of rainbow trapping with topological wave physics has very recently been achieved [24,51–53]; we take these concepts to exemplify the advantages of the proposed design in tailoring edge waves.

II. DESIGN PARADIGM

To breathe life into the concept of hierarchical metamaterial structures for robust edge wave control, we choose a tetrachiral lattice with multiple lateral resonators that act as added masses (see Fig. S1 in the Supplemental Material [54]); this choice is motivated by the broad band gaps of the structure, the square geometry for fabrication, and the attraction of employing both the beneficial characteristics of chiral lattices, combined with those of a graded system. We only utilize this structure in the low-frequency range (up to 1 kHz), in which the resonance of the lateral resonators is not achieved, and so they act as added masses. The combination of the chirality with the hierarchical mass variation brings about interesting dynamical phenomena at low frequencies. The lattice possesses topological properties, as discussed in later sections, meaning that in a specific band gap, it fosters two coincident edge
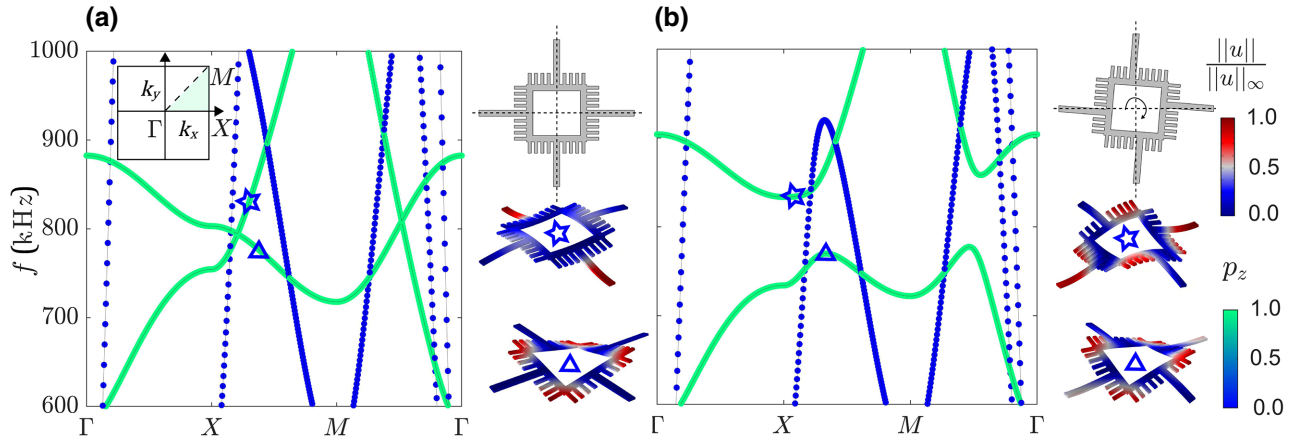
FIG. 2. The vertically polarized dispersion relation for (a) the symmetric (degenerate) and (b) the shifted (lifted degeneracy) cell, with $p4m$ and $p4$ plane symmetry (wallpaper) groups, respectively, computed along the irreducible Brillouin zone (IBZ) shown in the inset. The color map of the dispersion curves shows the relative polarization of the cell, denoted by p_z, with green points corresponding to vertical (out-of-plane) polarization, while blue refers to horizontal (in-plane) polarization. Only the vertically polarized (green) curves are relevant, as the structure is excited to only generate out-of-plane wave propagation. The points of accidental degeneracy are lifted when the mirror symmetry is broken and the flexural waves now exhibit a band gap (b). The geometry and eigensolutions of the cells involved are also shown, with a displacement color map from blue to red denoting the total absolute displacement field normalized with respect to its maximum. In the symmetric configuration, flexural and torsional waves are decoupled (blue star and triangle) (a); they couple when mirror symmetry is broken (b).

modes protected from the scattering phenomena arising due to the presence of defects. The implementation of the lateral masses is key to tailoring not only the band gap that contains the desired edge modes but also the edge modes themselves, granting the necessary design freedom needed to engineer protected edge modes with the desired dispersion characteristics. Figure 1 shows the final structure designed and used in experiments. We illustrate both the numerical simulation with an emission color map [Fig. 1(a)] and the experimental results [Fig. 1(b)] measured on the real specimen using a Polytec three-dimensional (3D) scanning laser Doppler vibrometer (SLDV) that scans the entire lattice. The structure shows a well-localized edge mode at around 670 Hz. The experimental velocity field in the bulk and the edge is also reported in the frequency range of interest, to visualize the confined nature of such edge states [Fig. 1(c)].

To show the illustrative design process and the relationship of the observed edge states with topologically protected states, we first consider simpler demonstrative unit cells before presenting the final structure that is both investigated numerically and experimentally characterized, as shown in Fig. 1. In particular, the importance of mirror symmetry, the creation of Dirac points, and the opening (or "gapping") of them by breaking mirror symmetry is illustrated in the cells shown in Fig. 2. These cells exemplify the importance of topology and we then tune the band gap to lower frequencies by adjusting the mass and arm positions with an intermediate cell along the design path illustrated in Fig. 3. The final cell, with its optimal

design, is shown in Fig. 4 and a ribbon geometry is used to demonstrate the edge states.

III. CELL TOPOLOGY

We design the lattice to control flexural-wave propagation, as they are ideal candidate waves for energy transport at low frequency and can be easily excited. To engineer topologically protected edge modes, it is first necessary to find and analyze a unit cell that is then periodically repeated to create an infinite lattice (the bulk medium); this is amenable to Floquet-Bloch theory and one extracts dispersion relations that relate the frequency to the Bloch wave number; the geometry with which we start (see Fig. 2) has points of degeneracy in the dispersion relation, i.e., band crossings. These points are necessary for the creation of a bulk band gap, i.e., a band of frequencies for the infinite lattice in which waves do not propagate, which is generated by lifting the degeneracy through the coupling of the two modes. The cell shown in Fig. 2(a) has a dispersion relation that shows two points of so-called accidental degeneracy [34,36] in the range X–M and M–Γ, which denotes the high symmetry directions of the irreducible Brillouin zone (IBZ), as shown in the inset of Fig. 2(a). Since we are interested in the out-of-plane behavior, we color the dispersion curves by using the vertical polarization p_z, computed as the ratio between the maximum out-of-plane and in-plane displacement along the entire unit cell domain to delineate the in- and out-of-plane-dominated modes.

For the out-of-plane modes upon which we concentrate, the green dispersion curves, we utilize both flexural and torsional waves, i.e., waves with rotational polarization along the cell axes; in the perfectly symmetric case, these are decoupled but they combine when a mirror symmetry breaking is introduced. The degeneracy is marked by the intersection of the flexural and torsional waves, both marked in green in the dispersion curves of Fig. 2(a), which do not interact when the cell is fourfold rotational and mirror symmetric, i.e., a $p4m$ wallpaper group. This is seen in Fig. 2(a), where the flexural eigensolution (blue star) is not coupled to the torsional one (blue triangle) and the modes have clearly distinct symmetries. To create the bulk band gap that hosts the protected edge mode, the degeneracy has to be lifted by coupling the two modes. To do so, the beams that connect the squared cells are shifted in an asymmetric way, thereby breaking mirror symmetry, which in turn requires a rotation of the base cell to guarantee periodicity conditions; the breaking of mirror symmetry is essential in terms of opening the band gap [34,36]. This cell, with $p4$ symmetry group, is shown in Fig. 2(b) together with the associated dispersion curves, where we note the lifted degeneracy that now opens a band gap as we require. Contrary to the symmetric configuration in Fig. 2(a), the two eigensolutions (blue star and triangle) are now coupled, i.e., flexural and torsional waves are mixed together. This in turn eliminates the accidental degeneracy of the two modes shifting the dispersion relations, uniting them and creating the band gap of interest; this rotated cell already has topological protection given by the mode coupling generated by removing the mirror

symmetry of the cell. To determine whether an edge mode, situated in the bulk band gap, is topologically protected, we evaluate the Berry curvature [29,55,56].

The Berry curvature, $\Omega_n(\mathbf{k})$, given by (using bra-ket notation)

$$\Omega_n(\mathbf{k}) = -\nabla_k \times \mathfrak{Im}\{\langle \mathbf{u}_n(\mathbf{k}) \mid \nabla_k \mid \mathbf{u}_n(\mathbf{k})\rangle\}, \quad (1)$$

evaluates how, in the reciprocal space, the eigensolution rotates in the Brillouin zone (BZ); as a consequence the Chern number, C_n, given by

$$C_n = \frac{1}{2\pi} \int_{BZ} \Omega_n(\mathbf{k}) d^2 k, \quad (2)$$

counts how many times the Berry curvature has critical points over the entire zone [57].

In these equations, $\mathbf{k}$ is the wave vector, $\mathbf{u}_n(\mathbf{k})$ is the eigenvector associated with a certain $\mathbf{k}$ and with the nth mode, and $\mathbf{u}_n(\mathbf{k})$ is a vector containing all the normalized displacements of the nodes (from the finite-element analysis) or the nodal displacement of the masses for lumped systems. The integration of the Berry curvature has to be evaluated over the complete first Brillouin zone (FBZ), without counting the edges of the zone twice, to obtain the Chern number. In certain cases, a simplified calculation of the Chern number is performed near the critical points, thus giving the valley Chern number C_v, but generally these type of calculations are not precise and are heavily dependent on the discretization of the wave vector and mainly over strong space-inversion symmetry breaking [58]. Here, we assess the presence of the critical points
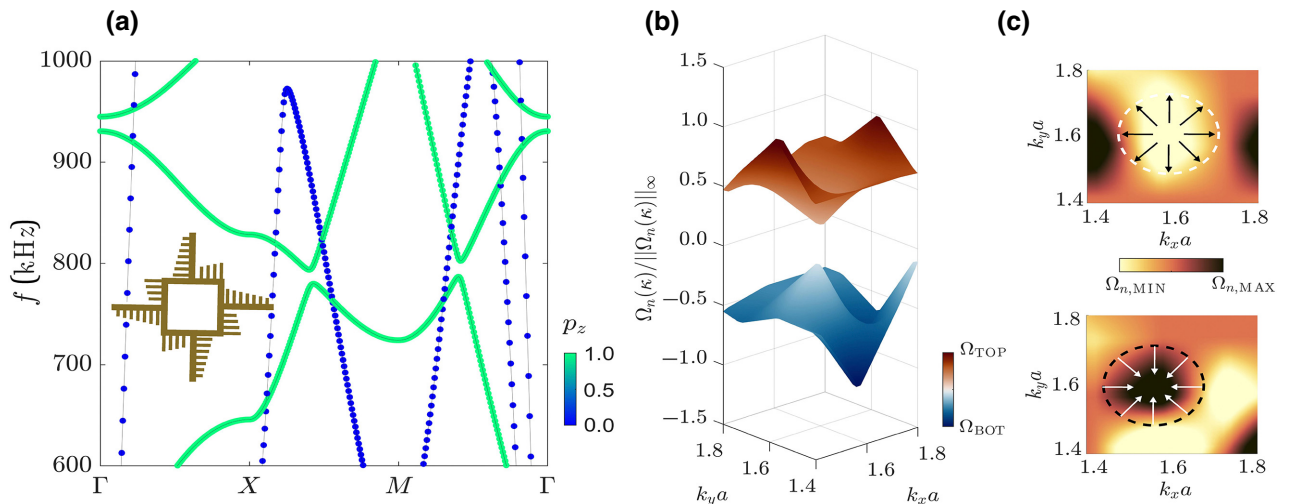

FIG. 3. (a) The vertically polarized dispersion relation of the shifted cell that possesses the $p4$ symmetry group. The cell is topologically equivalent to the degenerate case seen in Fig. 2. The cell geometry is shown in the inset. (b) A 3D surface view of the Berry curvatures of the top and bottom bands near the lifted degeneracy point shown in (a). The opposite sign of the cones along the bottom and top dispersion branches in the neighborhood of the lifted degeneracy identifies a critical point. This underpins a valley Hall analog, which guarantees topologically protected modes within the bulk band gap. (c) The top view of the Berry-curvature cones of the two modes. The gradient of the field is reported with white and black arrows, emphasizing the opposite sign of the top and bottom cones.
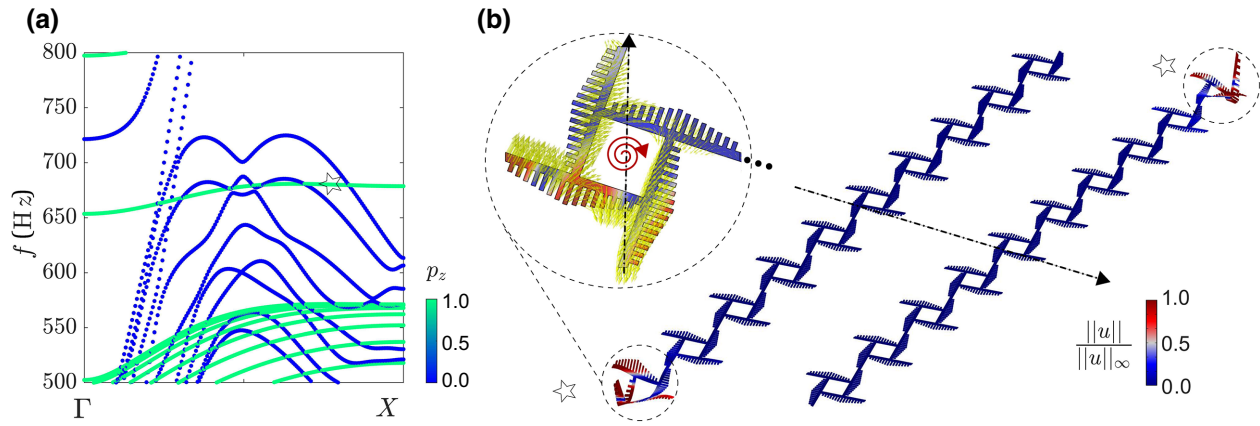
FIG. 4. (a) The vertically polarized dispersion relation of the ribbon. The star indicates the degenerate edge modes. (b) The corresponding eigensolution is reported. The results are obtained considering a ribbon made of ten cells, periodically repeated along the arrow direction. An enlargement of the edge cell of the ribbon is shown with the associated magnitude of the displacement field (with a red and blue color map). The arrow denotes the direction along which periodic boundary conditions are imposed, while the dots denote the sequence of nine cells in the ribbon. On top of this, the curl of the displacement field is superimposed, with yellow arrows showing the chiral nature of the motion, with opposite chirality between the left and right boundaries.

of the Berry curvature, given that these points are present concurrently with the band gap only when the modes that create the band gap support topologically protected modes. To achieve the maximal band-gap width, the shifts of the main beams have to be maximized, thereby increasing the coupling of the two modes; the maximum shift corresponds to the cell that we employ. Furthermore, the added lateral masses are positioned on just one side of the beams, to broaden the band gap and tune it to lower frequencies, given the strong coupling effect of mass eccentricity.

The calculations of the Berry curvature are performed over the cell reported in the inset of Fig. 3(a). This cell still maintains a $p4$ symmetry group as the final cell of the lattice and the cones in the dispersion curves [Fig. 3(a)] are well identified due to the breaking of mirror symmetries. In this cell, the lateral masses are now positioned over only one side of the connecting beams, which allows us to emphasize the lifted degeneracy and to increase the band-gap width. With regard to the topological protection of the edge mode, Fig. 3(b) shows the Berry curvature in the vicinity of the critical points, evaluated through Eq. (1) over the opening and closing eigensolutions. To do so, the eigenvectors $\mathbf{u}_n(\mathbf{k})$ associated with the two modes are extracted from the eigensolutions over the full Brillouin zone (BZ) of the cell in the reciprocal space. The numerical calculation is performed by means of the ABAQUS® finite-element software, showing the two mirrored cones associated with the two modes that create the band gap. We note that the Berry curvature in a neighborhood of the lifted degeneracy has cones of opposite sign along the bottom and top dispersion branches. This allows us to obtain a valley Hall analog that ensures topologically protected modes within the bulk band gap. To better visualize this

result, Fig. 3(c) shows top and bottom views of the Berry curvature, together with the gradient of the field.

IV. PROTECTED EDGE MODE

Having analyzed the band gap and its topological properties, we now focus on protected edge modes; these modes, existing within the bulk band gap, are a combination of torsional and flexural waves. They propagate only at the boundary of the lattice and are heavily localized on the edge cells: they decay abruptly in the bulk. Moreover, the two edge modes are identical but propagate along opposite directions. They are analyzed numerically by performing a dispersion analysis on a ribbon made of one line of repeated cells. In this paper, we opt for a ribbon with ten cells; we note that the dispersion branch of the edge mode converges to the same result from even just five cells but we consider ten cells to better illustrate the strong confinement of the eigensolution. The dispersion analysis is performed considering the ribbon in Fig. 4(b), where periodic boundary conditions are applied along the direction denoted by the dashed arrow. Figure 4 reports the results of the analysis conducted over the final, most staggered, configuration. Since the lifted eigensolution is preserved by rotation operators [59], the band gap is enlarged while preserving topological protection. The two modes are coincident but each of them is localized only to one of the two edges. The edge-mode dispersion additionally shows that the propagating mode is very slow given the near-zero group velocity across most of the IBZ. This is useful for energy harvesting or sensing, since slow energy transport along the edge gives a larger interaction time with the harvesting or detection system to capture energy or
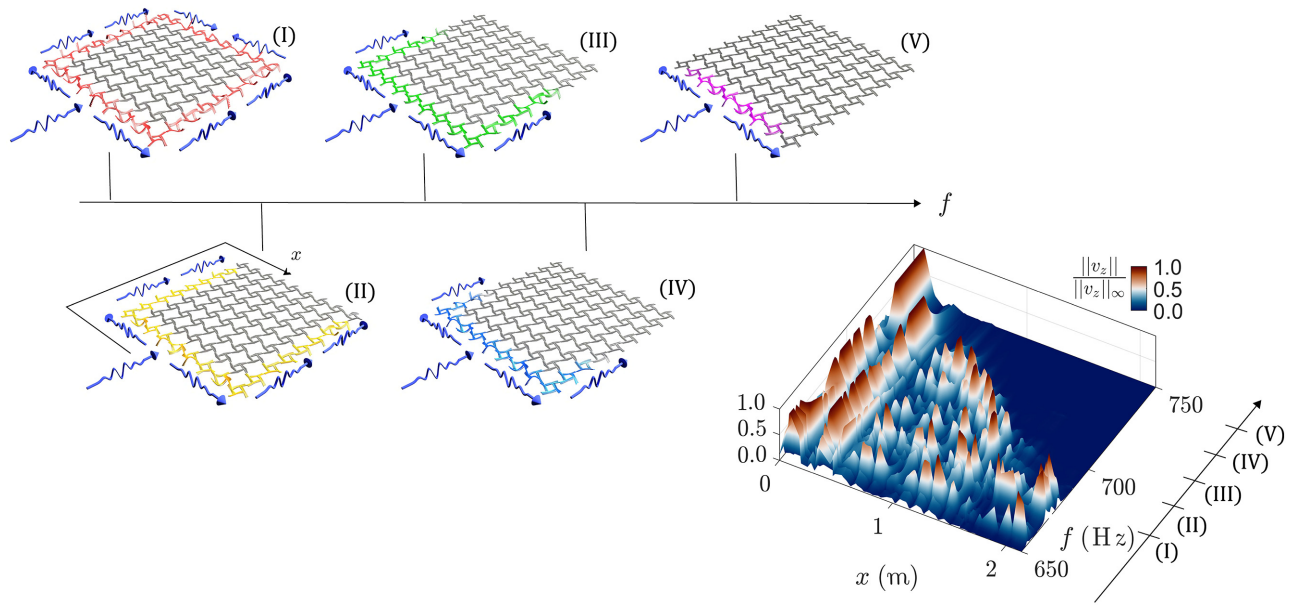
FIG. 5. The results of the rainbow effect over the topologically protected edge mode. Different renderings of the numerical results are reported with a color coating that shows where the waves, characterized by different frequency components, get blocked and confined. The blue arrows show the input wave and its propagation direction on the lattice. The numbering refers to the respective frequencies, organized in ascending order. The localization and the rainbow effect are shown with a corresponding time-domain fast Fourier transform (FFT) computed over the unwrapped edge.

signal data [45]. Figure 4 also reports the curl of the displacement field, which shows, as does the cell itself, a well-defined chirality. This chiral nature of the mode supports the idea of the topologically protected mode [24], given that the wave field is confined on the edge. The edge-mode robustness is also corroborated by time-domain analyses via implicit time integration [60] on a defected structure (see Fig. S2 in the Supplemental Material [54]), where we note the existence of such an edge mode even in presence of large defects. Moreover, the existence of the edge mode is confirmed by Fourier transforming the time-domain results (see Fig. S4 in the Supplemental Material [54]).

V. RAINBOW EDGE MODE

Having analyzed the edge-mode properties and behavior, we now focus on modifying its characteristics, namely its group and phase velocities and the position of the zero-group-velocity point within the Brillouin zone. The aim is to tailor these properties without modifying the total added mass given by the lateral resonators, so that the band gap that fosters the protected mode is not altered between the different cells. In the cases analyzed here, we define the functions for the change in length of the masses in such a way that the added mass is kept constant, regardless of the spatial distribution. In this way, the location of the edge mode remains confined in the protected bulk band gap, without any significant frequency shift; thus, topological

protection is preserved. The control over the dispersion properties of the edge mode is necessary to engineer its behavior in the frequency range of interest. The change of the dispersion branch is then used to progressively modify the propagating wave characteristics, e.g., to create grading effects, on the edge of the lattice (see Fig. S3 in the Supplemental Material [54]). We then demonstrate the advantages of the proposed design concept, creating the rainbow effect as a meaningful example. The rainbow effect engineered in this work is constructed through the use of five different cells with the same geometry, except from the grading of masses. Specifically, we adopt the following linear grading of lengths: $l_1 \in [13, 5]$ mm, $l_2 \in [10.7, 6.5]$ mm (inverse grading), $l_3 \in [8.7, 8.7]$ mm (periodic), $l_4 \in [7.2, 10.4]$ mm, and $l_5 \in [5, 13]$ mm (direct grading). The configurations are chosen carefully following the set of rules defined above and maintaining the notion of an adiabatic change of the homogenized properties of the lattice, i.e., considering a slow variation of the fundamental Bloch mode of each cell along the spatial dimension [61,62]. The edge rainbow structure is also assembled following the idea of having two symmetric directions of propagation of the input edge wave, meaning that the overall lattice has a mirror symmetry group. The lattice mirror plane is positioned exactly at the center of one of the edges, where we apply the input wave.

Within the lattice, in the bulk, we keep the spatial distribution of the masses unchanged. This choice does not disrupt the propagating edge mode because the bulk band

gap supports the edge mode even when the lateral masses are modified, highlighting that the spatial distribution can be defined and implemented by just considering the edge-mode dispersion branch. Figure 5 reports the results obtained from a finite-element analysis on the described structure. It shows how a broadband input generated at the center of one edge propagates at the boundary of the structure, being confined at different spatial positions depending on its frequency. Figure 5 also highlights the localization of frequency components with respect to spatial positions over the unwrapped edge, which is a distinctive property of the rainbow effect [43].

VI. CONCLUSIONS

We show, both numerically and experimentally, the physics of a hierarchical tetrachiral lattice that fosters topologically protected edge modes. The edge mode is engineered to obtain full control over its propagation in both space and time. Moreover, as a meaningful example, we also obtain the topological rainbow effect by modifying the dispersion properties of the edge mode along the boundary of the lattice, granting the localization of different frequency components along the edge. This control over the dispersion properties is obtained due to microelements added to the cell (lateral masses), without changing the shape or the added mass. Future developments will assess the behavior of the structure at higher frequencies, i.e., when the resonators begin to work dynamically at resonance.

ACKNOWLEDGMENTS

[1] A. B. Khanikaev, S. H. Mousavi, W.-K. Tse, M. Kargarian, A. H. MacDonald, and G. Shvets, Photonic topological insulators, Nat. Mater. **12,** 233 (2013).

[2] L. Lu, J. Joannopoulos, and M. Soljačić, Topological photonics, Nat. Photonics **8,** 821 (2014).

[3] A. B. Khanikaev, R. Fleury, S. H. Mousavi, and A. Alù, Topologically robust sound propagation in an angular-momentum-biased graphene-like resonator lattice, Nat. Commun. **6,** 1 (2015).

[4] A. B. Khanikaev and G. Shvets, Two-dimensional topological photonics, Nat. Photonics **11,** 763 (2017).

[5] S. H. Mousavi, A. B. Khanikaev, and Z. Wang, Topologically protected elastic waves in phononic metamaterials, Nat. Commun. **6,** 1 (2015).

[6] S. D. Huber, Topological mechanics, Nat. Phys. **12,** 621 (2016).

[7] J. E. Moore, The birth of topological insulators, Nature **464,** 194 (2010).

[8] M. Z. Hasan and C. L. Kane, Colloquium: Topological insulators, Rev. Mod. Phys. **82,** 3045 (2010).

[9] H. Nassar, B. Yousefzadeh, R. Fleury, M. Ruzzene, A. Alù, C. Daraio, A. N. Norris, G. Huang, and M. R. Haberman, Nonreciprocity in acoustic and elastic materials, Nat. Rev. Mater. **5,** 667 (2020).

[10] W. Cheng, E. Prodan, and C. Prodan, Experimental Demonstration of Dynamic Topological Pumping across Incommensurate Bilayered Acoustic Metamaterials, Phys. Rev. Lett. **125,** 224301 (2020).

[11] P. Wang, L. Lu, and K. Bertoldi, Topological Phononic Crystals with One-Way Elastic Edge Waves, Phys. Rev. Lett. **115,** 104302 (2015).

[12] M. P. Makwana and R. V. Craster, Geometrically navigating topological plate modes around gentle and sharp bends, Phys. Rev. B **8,** 1 (2018).

[13] M. Miniaci, R. K. Pal, B. Morvan, and M. Ruzzene, Experimental Observation of Topologically Protected Helical Edge Modes in Patterned Elastic Plates, Phys. Rev. X **8,** 1 (2018).

[14] J. Cha, K. W. Kim, and C. Daraio, Experimental realization of on-chip topological nanoelectromechanical metamaterials, xxx **564,** 229 (2018).

[15] M. V. Berry, Quantal phase factors accompanying adiabatic changes, Proc. R. Soc. Lond. A 392, 224301 (1984).

[16] D. Xiao, M. C. Chang, and Q. Niu, Berry phase effects on electronic properties, Rev. Mod. Phys. **82,** 1959 (2010).

[17] M. Xiao, G. Ma, Z. Yang, P. Sheng, Z. Q. Zhang, and C. T. Chan, Geometric phase and band inversion in periodic acoustic systems, Nat. Phys. **11,** 240 (2015).

[18] J. Yin, M. Ruzzene, J. Wen, D. Yu, L. Cai, and L. Yue, Band transition and topological interface modes in 1D elastic phononic crystals, Sci. Rep. **8,** 1 (2018).

[19] Y. Hatsugai, Chern Number and Edge States in the Integer Quantum Hall Effect, Phys. Rev. Lett. **71,** 3697 (1993).

[20] A. Souslov, B. C. Van Zuiden, D. Bartolo, and V. Vitelli, Topological sound in active-liquid metamaterials, Nat. Phys. **13,** 1091 (2017).

[21] S. Shankar, A. Souslov, M. J. Bowick, M. C. Marchetti, and V. Vitelli, Topological active matter, Nat. Rev. Phys. **4,** 380 (2022).

[22] F. D. M. Haldane, Model for a Quantum Hall Effect without Landau Levels: Condensed-Matter Realization of the "Parity Anomaly", Phys. Rev. Lett. **61,** 2015 (1988).

[23] R. Süsstrunk and S. D. Huber, Observation of phononic helical edge states in a mechanical topological insulator, Science **349,** 47 (2015).

[24] G. J. Chaplain, J. M. De Ponti, G. Aguzzi, A. Colombi, and R. V. Craster, Topological Rainbow Trapping for Elastic Energy Harvesting in Graded Su-Schrieffer-Heeger Systems, Phys. Rev. Appl. **14,** 054035 (2020).

[25] C. L. Kane and E. J. Mele, Quantum Spin Hall Effect in Graphene, Phys. Rev. Lett. **95,** 226801 (2005).

[26] B. A. Bernevig, T. L. Hughes, and S. C. Zhan, Quantum spin Hall effect and topological phase transition in HgTe quantum wells, Science **314,** 1757 (2006).

[27] D. Xiao, W. Yao, and Q. Niu, Valley-Contrasting Physics in Graphene: Magnetic Moment and Topological Transport, Phys. Rev. Lett. **99,** 236809 (2007).

[28] J. Jung, F. Zhang, Z. Qiao, and A. H. MacDonald, Valley-Hall kink and edge states in multilayer graphene, Phys. Rev. B **84,** 075418 (2011).

[29] R. K. Pal and M. Ruzzene, Edge waves in plates with resonators: An elastic analogue of the quantum valley Hall effect, New J. Phys. **19,** 1 (2017).

[30] J. Vila, R. K. Pal, and M. Ruzzene, Observation of topological valley modes in an elastic hexagonal lattice, Phys. Rev. B **96,** 134307 (2017).

[31] S. S. Ganti, T. W. Liu, and F. Semperlotti, Topological edge states in phononic plates with embedded acoustic black holes, J. Sound Vib. **466,** 1 (2020).

[32] A. Bacigalupo and L. Gambarotta, Simplified modelling of chiral lattice materials with local resonators, Int. J. Solids Struct. **83,** 126 (2016).

[33] A. Bacigalupo, A. Gnecco, M. Lepidi, and L. Gambarott, Optimal design of low-frequency band gaps in anti-tetrachiral lattice meta-materials, Compos. B Eng. **115,** 341 (2017).

[34] W. Y. He and C. Chan, The emergence of Dirac points in photonic crystals with mirror symmetry, Sci. Rep. **5,** 1 (2015).

[35] M. P. Makwana and G. J. Chaplain, Tunable three-way topological energy-splitter, Sci. Rep. **9,** 1 (2019).

[36] M. P. Makwana, R. V. Craster, and S. Guenneau, Topological beam-splitting in photonic crystals, Opt. Express **27,** 1 (2019).

[37] M. P. Makwana, N. Laforge, R. V. Craster, G. Dupont, S. Guenneau, V. Laude, and M. Kadic, Experimental observations of topologically guided water waves within non-hexagonal structures, Appl. Phys. Lett. **116,** 1 (2020).

[38] R. Drost, T. Ojanen, A. Harju, and P. Liljeroth, Topological states in engineered atomic lattices, Nat. Phys. **13,** 668 (2017).

[39] W. Jiang, M. Kang, H. Huang, H. Xu, T. Low, and F. Liu, Topological band evolution between Lieb and Kagome lattices, Phys. Rev. B **99,** 125131 (2019).

[40] W. P. Syam, W. Jianwei, B. Zhao, I. Maskery, W. Elmadih, and R. Leach, Design and analysis of strut-based lattice structures for vibration isolation, Precis. Eng. **52,** 494 (2018).

[41] B. Zhao, H. R. Thomsen, J. M. De Ponti, E. Riva, B. Van Damme, A. Bergamini, E. Chatzi, and A. Colombi, A graded metamaterial for broadband and high-capability piezoelectric energy harvesting, Energy Convers. Manag. **269,** 116056 (2022).

[42] Y. Xie, T.-H. Tsai, A. Konneker, B.-I. Popa, D. J. Brady, and S. A. Cummer, Single-sensor multispeaker listening with acoustic metamaterials, PNAS **112,** 10595 (2015).

[43] K. L. Tsakmakidis, A. D. Boardman, and O. Hess, "Trapped rainbow" storage of light in metamaterials, Nature **450,** 397 (2007).

[44] Q. Gan, Y. Gao, K. Wagner, D. Vezenov, Y. J. Ding, and F. J. Bartoli, Experimental verification of the rainbow trapping effect in adiabatic plasmonic gratings, PNAS **108,** 5169 (2011).

[45] G. J. Chaplain, D. Pajer, J. M. De Ponti, and R. V. Craster, Delineating rainbow reflection and trapping with applications for energy harvesting, New J. Phys. **22,** 063024 (2020).

[46] X. Ni, Y. Wu, Z. G. Chen, L. Y. Zheng, Y. L. Xu, P. Nayar, X. P. Liu, M. H. Lu, and Y. F. Chen, Acoustic rainbow trapping by coiling up space, Sci. Rep. **4,** 1 (2014).

[47] J. M. De Ponti, L. Iorio, E. Riva, R. Ardito, F. Braghin, and A. Corigliano, Selective Mode Conversion and Rainbow Trapping via Graded Elastic Waveguides, Phys. Rev. Appl. **16,** 034028 (2021).

[48] A. Colombi, D. Colquitt, P. Roux, S. Guenneau, and R. V. Craster, A seismic metamaterial: The resonant metawedge, Sci. Rep. **6,** 1 (2016).

[49] J. M. De Ponti, A. Colombi, R. Ardito, F. Braghin, A. Corigliano, and R. V. Craster, Graded elastic metasurface for enhanced energy harvesting, New J. Phys. **22,** 013013 (2019).

[50] G. J. Chaplain, J. M. De Ponti, A. Colombi, R. Fuentes-Dominguez, P. Dryburg, D. Pieris, R. J. Smith, A. Clare, M. Clark, and R. V. Craster, Tailored elastic surface to body wave Umklapp conversion, Nat. Commun. **11,** 1 (2020).

[51] B. Ungureanu, M. P. Makwana, R. V. Craster, and S. Guenneau, Localizing Elastic Edge Waves via the Topological Rainbow Effect, Phys. Rev. Appl. **15,** 014057 (2021).

[52] C. Lu, Y.-Z. Sun, C. Wang, H. Zhang, W. Zhao, X. Hu, M. Xiao, W. Ding, Y.-C. Liu, and C. T. Chan, On-chip nanophotonic topological rainbow, Nat. Commun. **13,** 1 (2022).

[53] H. Zhang, S. Elshahat, C. Wang, and C. Lu, Perspective on the topological rainbow, Appl. Phys. Lett. **119,** 230505 (2021).

[54] See the Supplemental Material at http://link.aps.org/supplemental/10.1103/PhysRevApplied.19.034079 for more details on the underlying physics of the protected edge mode in the hierarchical metamaterial.

[55] R. Resta, Manifestations of Berry's phase in molecules and condensed matter, J. Condens. Matter Phys. **12,** R107 (2000).

[56] S. S. Ganti, T.-W. Liu, and F. Semperlotti, Topological edge states in phononic plates with embedded acoustic black holes, J. Sound Vib. **466,** 115060 (2020).

[57] T. Fösel, V. Peano, and F. Marquardt, L lines, C points and Chern numbers: Understanding band structure topology using polarization fields, New J. Phys. **19,** 115013 (2017).

[58] H. Zhu, T.-W. Liu, and F. Semperlotti, Design and experimental observation of valley-Hall edge states in diatomic-graphene-like elastic waveguides, Phys. Rev. B **97,** 174301 (2018).

[59] J. Lu, C. Qiu, L. Ye, X. Fan, M. Ke, F. Zhang, and Z. Liu, Observation of topological valley transport of sound in sonic crystals, Nat. Phys. **13**, 369 (2017).

[60] H. M. Hilber, T. J. R. Hughes, and R. L. Taylor, Improved numerical dissipation for time integration algorithms in structural dynamics, Earthq. Eng. Struct. Dyn. **5**, 283 (1977).

[61] O. Schnitzer, Waves in slowly varying band-gap media, SIAM J. Appl. Math. **77**, 1516 (2017).

[62] S. G. Johnson, P. Bienstman, M. A. Skorobogatiy, M. Ibanescu, E. Lidorikis, and J. D. Joannopoulo, Adiabatic theorem and continuous coupled-mode theory for efficient taper transitions in photonic crystals, Phys. Rev. E **66**, 066608 (2002).